Journal of Power Sources 196 (2011) 5761–5768

Contents lists available at ScienceDirect

Journal of Power Sources

journal homepage: www.elsevier.com/locate/jpowsour

Electrochemical micro-capacitors of patterned electrodes loaded with manganese oxide and carbon nanotubes

Chi-Chie Liu [a], Dah-Shyang Tsai [a,*], Wen-Hung Chung [a], Kuan-Wei Li [b], Kuei-Yi Lee [b], Ying-Sheng Huang [b]

[a] Department of Chemical Engineering, National Taiwan University of Science and Technology, 43, Keelung Road, Section 4, Taipei 10607, Taiwan
[b] Department of Electronic Engineering, National Taiwan University of Science and Technology, Taipei 10607, Taiwan

ARTICLE INFO

Article history:
Received 13 November 2010
Received in revised form 27 January 2011
Accepted 17 February 2011
Available online 24 February 2011

Keywords:
Electrochemical capacitor
Interdigital electrode
Manganese oxide
Carbon nanotubes
Vertical alignment
Polarization loss

ABSTRACT

MnO_2 and carbon nanotubes (CNT) composite electrodes have been built on the interdigital stack layers of Fe–Al/SiO_2 and Fe–Al/Au/Ti/SiO_2 for the electrochemical micro-capacitors, using photolithography and thin-film technologies. The electrode properties and the performance of micro-cells are measured and analyzed with cyclic voltammetry (CV), impedance spectroscopy, and galvanostatic charge/discharge test in 0.1 M Na_2SO_4 electrolyte. The vertically aligned CNT, grown on Fe–Al/SiO_2, is more suitable for supporting the pseudocapacitive MnO_2 than the random CNT on Fe–Al/Au/Ti/SiO_2, but ohmic resistance of the former electrode is higher. We have prepared three cells on each stack layer with different electrode materials. The Ragone plot shows systematic variations in power and energy performance, reflecting their differences in electrode structure and polarization loss. The asymmetric cell of a pseudocapacitive positive electrode, loaded with MnO_2 and CNT, exhibits a small IR drop and a high specific energy during discharge. Built on Fe–Al/SiO_2, this asymmetric cell discharges at specific power 0.96 kW kg^{-1} with specific energy 10.3 Wh kg^{-1}; while on Fe–Al/Au/Ti/SiO_2, the asymmetric cell discharges at power 1.16 kW kg^{-1} with energy 5.71 Wh kg^{-1}.

© 2011 Elsevier B.V. All rights reserved.

1. Introduction

The electrochemical capacitor (or ultracapacitor) stores its electrical charges at the interface of electrolyte and electrode by means of double-layer capacitance or pseudocapacitance. This capacitor occupies a unique position between regular capacitors and batteries, because of its collective features of sufficient energy storage, long cycle life, and pulse power delivery. When used in conjunction with batteries, the ultracapacitor is proven excellent in fulfilling the peak current requirement and lengthening the battery life. Through a proper cell design, it is also capable to serve as a stand-alone unit for the energy grid to smooth the power surge and provide limited storage capacity [1–5]. Recently, the miniaturized electrochemical capacitors are suggested to be the power source for micro-electromechanical systems (MEMS), because of its small dimensions and high energy density. The electrochemical micro-capacitors based on conducting polymers or polymeric electrolytes are more suitable for flexible electronics, prepared via filtration, printing or spin coating [6–9]. Those micro-capacitors, built on rigid substrates of silicon or silica glass, are generally fabricated using the thin-film technologies for semiconductor, such as photolithography, chemical and physical vapor depositions [10–14], or laser direct write [15,16].

X-ray amorphous manganese oxide (MnO_2) in the hydrated form is widely known for its high pseudocapacitance [17–19], broad potential window as the positive electrode [20], environmental friendliness, and low material cost. The specific capacitance of MnO_2 powder has been reported 150–440 F g^{-1}, depending on the synthesis method and crystal structure [21–23]. The reported values for the MnO_2 thin film are much higher, 698 F g^{-1} for a 1.05 μg cm^{-2} film on nickel foil, 1380 F g^{-1} for the thin film on platinum foil [17,24]. Its main drawback is the poor electrical conductivity which restricts its capacitive performance. Mixing with conductive carbonaceous materials of high surface area improves the less ideal conductivity. To this end, researchers have demonstrated that a loading of 10–50 wt% carbon nanotubes (CNT) in the MnO_2–CNT composite effectively upgrades the conductivity and the capacitance [25]. Other composites, such as MnO_2/active carbon, MnO_2/carbon aerogel, MnO_2/CNT coaxial arrays [26–29], has been intelligently designed and synthesized, leading to further improvement on the properties.

In this work, we fabricate several ultracapacitors of interdigital electrode using the standard thin-film technologies. These micro-cells, having a planar configuration, are convenient to integrate with MEMS devices. We measure the electrode properties using cyclic voltammetry (CV), electrochemical impedance

* Corresponding author. Tel.: +886 2 27376618; fax: +886 2 27376644.
E-mail address: dstsai@mail.ntust.edu.tw (D.-S. Tsai).

0378-7753/$ – see front matter © 2011 Elsevier B.V. All rights reserved.
doi:10.1016/j.jpowsour.2011.02.050

spectroscopy (EIS), and evaluate the cell performance with galvanostatic charge/discharge tests. Among these cells, the asymmetric cell with a positive MnO_2 electrode stands out in power and energy output. The electrode polarization loss and the benefit of asymmetric design are analyzed and discussed.

2. Experimental

2.1. Electrode and cell fabrication

Interdigital and blanket CNT thin films were grown using thermal CVD on the stack layer of Fe–Al/SiO_2 or Fe–Al/Au/Ti/SiO_2 on a Si wafer. Patterning of the comb-like stack layer was performed with photolithography. The processing steps involved spin coating and developing using a photomask, a positive photoresist (AZ6112, Clariant), and its associated developer solution (AZ300MIF, AZ Electronic Materials). In preparing the Fe–Al/SiO_2 stack layer, a 5 nm thick aluminum layer and a 3 nm thick iron layer were sequentially deposited at 10^{-6} Torr, with an electron beam evaporator (PEVA-500E, Advanced System Technology). The Fe layer seeded the CNT growth, and the Al layer served as a growth buffer and current collector. Next, the photoresist was lifted off to produce the Fe–Al pattern on the 500 nm thick SiO_2 film. In preparing the Fe–Al/Au/Ti/SiO_2 stack layer, a 10 nm thick Ti film and a 20 nm thick Au film were sputtered, prior to depositing the Fe and Al layers, to reduce the electrical resistance of the stack layer. The gold thin film served as the current collector. This preparation procedure is not restricted to the oxidized Si wafer, also applicable on the commonly available alkali-free glass substrates. The wafer was only a choice of convenience.

To grow the CNT films, the substrates were placed in a horizontal tubular reactor of quartz glass, and acetylene (C_2H_2) was introduced at 750 °C to initiate the growth. The total growth time was 2 min under 4 Torr acetylene. According to Komukai and coworkers [29,30], the desirable CNT features, such as vertical alignment and high population density, relied on a proper match between the Al buffer layer and the Fe catalyst layer. In our practice, a combination of 5 nm Al layer, 3 nm Fe layer, and the above growth conditions yielded the preferred morphology. After CNT growth, the electrical wiring was made by applying a silver paste to glue a copper wire on the square lead area. This electrical contact was reinforced with an ARON inorganic adhesive. To complete a cell, all the surfaces, including the electrical contacts, wires, the lead areas, were insulated with Miccrostop lacquer (Pyramid Plastics, Tolber Division) so that only the comb area was exposed to the deaerated electrolyte 0.1 M Na_2SO_4 (pH 7).

Electrodeposition of MnO_2 on CNT was done in 0.2 M $MnSO_4$, using a galvanic square-wave pulse current and a three-electrode setup. The pH value of the electroplating solution was adjusted to 7.0 with dilute sulfuric acid and sodium sulfate. At a current density 5 mA cm^{-2}, one duty cycle of the pulse current consisted of 10 s on-time and 10 s off-time. One deposition run included 60 cycles. After MnO_2 deposition, the sample was dried at 50 °C in a laminar flow chamber overnight for further electrochemical analysis. The MnO_2 mass and the CNT mass of blanket films were weighed using a precision balance (BP211D, Sartorius). The CNT mass of the interdigital electrode was estimated using the mass per unit area of a blanket film grown in the same batch.

2.2. Cell notation

We denoted the electrode of blanket CNT film on Fe–Al/SiO_2 as bCNT, and that on Fe–Al/Au/Ti/SiO_2 as bCNT/Au. Likewise, the blanket manganese oxide-loaded CNT film on Fe–Al/SiO_2 was abbreviated as MnO_2–bCNT, and that on Fe–Al/Au/Ti/SiO_2 was MnO_2–bCNT/Au. The micro-capacitor was denoted, highlighting its active material. On Fe–Al/SiO_2, the symmetric cell of two CNT electrodes was CNT_CNT. When one CNT electrode was deposited with MnO_2 and designated as the positive electrode, the other CNT electrode was the negative electrode, the asymmetric cell was MnO_2(+)_CNT. When both CNT electrodes are loaded with MnO_2, the symmetric cell was abbreviated as MnO_2_MnO_2. By the same token, three cells on Fe–Al/Au/Ti/SiO_2 were denoted as CNT_CNT/Au, MnO_2(+)_CNT/Au, MnO_2_MnO_2/Au; individually.

2.3. Structure analysis and electrochemical measurements

Diffraction patterns of the electrode materials were recorded using an X-ray diffractometer (D/MAX-RC, Rigaku). Morphology of the electrodes was examined with a field-emission scanning electron microscope (SEM, JSM-6500F, JEOL). The EIS data were collected using a Solartron 1260 frequency analyzer. A platinum plate was the counter electrode, the blanket CNT or MnO_2–CNT electrode was the working electrode, whose potential was measured against an Ag/AgCl(sat. KCl) reference electrode (SR820, Radiometer Analytical). In the CV and galvanostatic charge/discharge experiments, we used a multichannel potentiostat (Solartron 1470). And one comb-like electrode was designated as the working (positive) electrode with its potential measured against the Ag/AgCl reference, the other was the counter (negative) electrode.

3. Results and discussion

3.1. Electrode morphology and structure

Under the joint effect of Fe seed and Al buffer, vertically aligned and densely populated multi-walled CNT were selectively grown on the Fe–Al/SiO_2 stack layer [30,31]. Fig. 1(a) shows a top-view image of the patterned comb-like CNT film. Each CNT finger is ~34 μm thick, 40 μm wide, and 2.7 mm long. These fingers are horizontally interspaced by a distance of 20 μm. One pattern has 30 fingers, occupying an area of 4 mm × 3 mm. Other linear dimensions are marked in the schematic diagram of Fig. 1(c). Fig. 1(b) presents a tilted-view image, showing those clear-cut CNT fingers stand on the substrate. We attribute this well-defined pattern to its vertical sidewall, whose details are revealed in Fig. 1(d) and (e). The sidewall is constructed by interwoven nanotubes, whose diameter varies between 10 and 20 nm. The nanotube orientation is different in the lower and upper section of sidewall, the nanotubes are largely aligned in the lower section, while randomly oriented in the upper section [30,31]. The number density of nanotubes is high, ~10^9 cm^{-2}. Fig. 1(f) shows that deposited MnO_2 globules suspend along the nanotubes. The globule size generally increases from bottom, ~2 μm, to top, ~6 μm.

The gold layer of Fe–Al/Au/Ti/SiO_2 enhances the current collecting capability, but interferes with the CNT growth. Fig. 1(g) presents a top-view image of the patterned CNT film on Fe–Al/Au/Ti/SiO_2. Its inset shows that this film consists of randomly oriented nanotubes, the average height of thin film is around 1.4 μm. We can grow a thicker CNT film, but choose not to do so, since randomly oriented nanotubes may extend into the nongrowth region and raise the probability of short circuit. Fig. 1(h) shows a tilted-view image of the MnO_2-deposited CNT film on Fe–Al/Au/Ti/SiO_2. The electrodeposited MnO_2 appears uniform.

Since the crystallite size of as-deposited MnO_2 is very small, no reflections are detected in its X-ray diffraction. The reflections of MnO_2 emerge after the sample was annealed at 200 °C for 1 h. Fig. 2 presents the diffraction pattern of an annealed MnO_2–CNT thin film on Fe–Al/Au/Ti/SiO_2, showing the signatures of β-MnO_2 crystal [32] along with those of the face-centered cubic Au crystal [33]. The

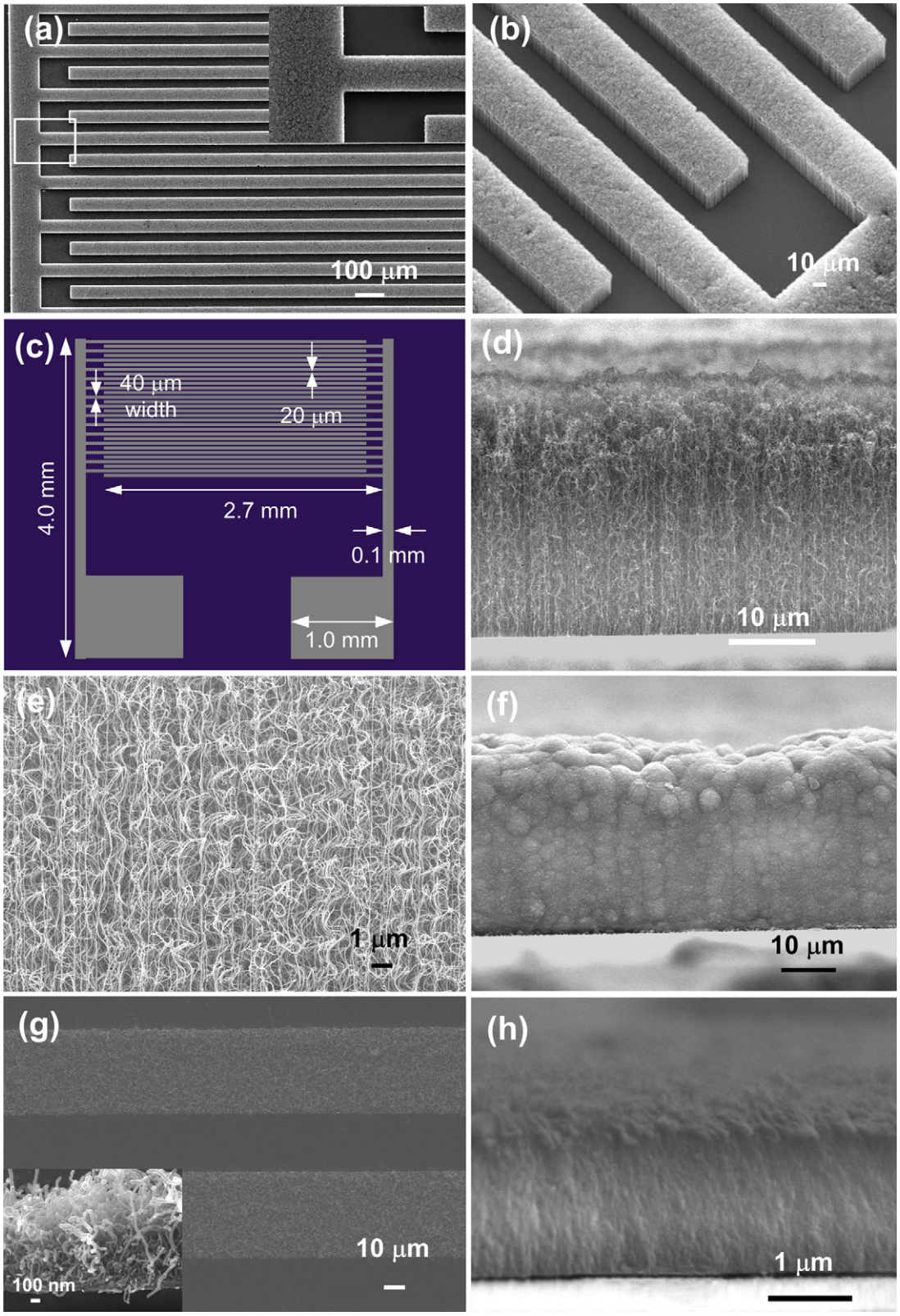

Fig. 1. (a)–(f) shows the morphology of patterned CNT and MnO_2–CNT films on Fe–Al/SiO_2. (a) Top-view SEM images of the CNT interdigital film and an enlarged image of its corners as the inset; (b) a 30° perspective view of the CNT film with vertical sidewall; (c) the designed comb-like pattern and its linear dimensions; (d) a cross-sectional image of the CNT film showing two sections of different alignment; (e) a SEM image showing alignment detail of nanotubes in the lower section; (f) a cross-sectional image of the 35 μm MnO_2–CNT film. (g) and (h) depict the morphology of CNT and MnO_2–CNT films on Fe–Al/Au/Ti/SiO_2; (g) a typical top-view image of patterned CNT film and the inset showing the cross-section of CNT film; (h) a cross-sectional image (10° tilted) of the MnO_2–CNT film.

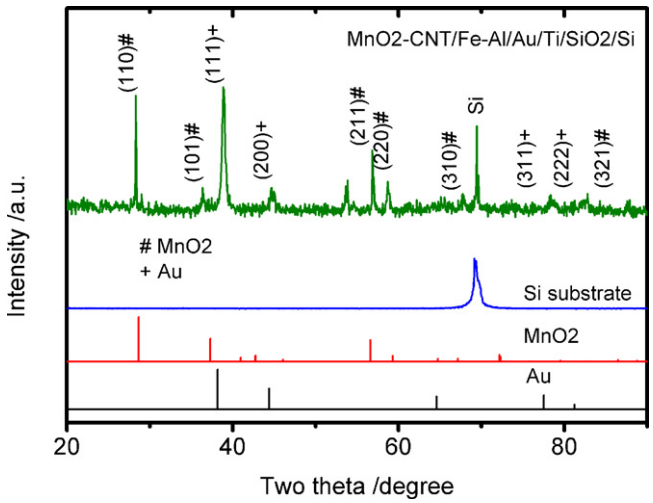

Fig. 2. X-ray diffraction pattern of MnO_2–bCNT/Au annealed at 200 °C, in contrast with the reflection lines for tetragonal β-MnO_2 crystal and Au crystal (JCPDS 81-2261 and 04-0784).

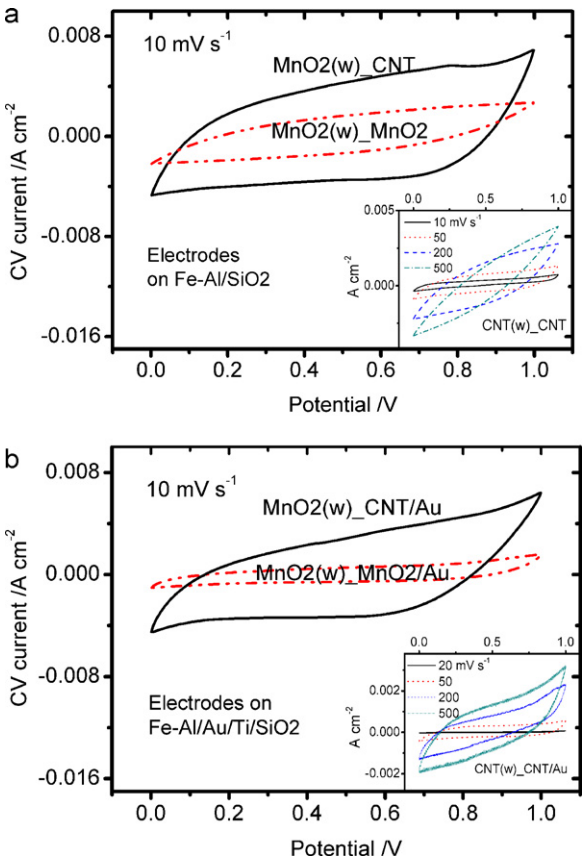

Fig. 3. (a) Voltammograms of MnO_2(w)_CNT and MnO_2(w)_MnO_2 at 10 mV s^{-1}, and the inset showing CV currents of CNT(w)_CNT at 10, 50, 200, and 500 mV s^{-1}. (b) Voltammograms of MnO_2(w)_CNT/Au and MnO_2(w)_MnO_2/Au at 10 mV s^{-1}, along with the inset for CV currents of CNT(w)_CNT/Au at 10, 50, 200, and 500 mV s^{-1}.

rutile phase of β-MnO_2 is featured with a tight crystal structure and small one dimensional tunnels for cation intercalation [34].

3.2. CV and impedance results

Fig. 3(a) presents the voltammograms for CNT(w)_CNT, MnO_2(w)_CNT, and MnO_2(w)_MnO_2 patterned electrodes, in which the working electrodes are marked with (w), and the other comb-like electrode serves as the counter electrode. Fig. 3(a) shows that the response current of MnO_2(w)_CNT is considerably higher than CNT(w)_CNT, and less tilted than MnO_2(w)_MnO_2, indicating that the deposited MnO_2 increases the capacitance and the electrode resistance. On the other hand, Fig. 3(b) shows the response current of MnO_2(w)_CNT/Au is lower than that of MnO_2(w)_CNT, since its MnO_2 and CNT loadings are less on the stack layer containing gold. Meanwhile the voltammogram of MnO_2(w)_MnO_2/Au is not as tilted as that of MnO_2(w)_MnO_2 because of the more conductive stack layer of Fe–Al/Au/Ti/SiO_2. The inset of Fig. 3(b) also shows a small response current and a less tilted voltammogram of CNT(w)_CNT/Au, compared with those of CNT(w)_CNT.

Table 1 lists the specific capacitance C_m values at various sweep rates, which are calculated using the following equation.

$$C_m = \frac{In_{CV}}{2\nu \times m_a \times \Delta V} \quad (1)$$

where In_{CV} is the area integral of voltammogram (A V cm^{-2}), ν the sweep rate (V s^{-1}), m_a the CNT and MnO_2 mass of working electrode (g cm^{-2}), ΔV the scanned potential window (V). The C_m values of MnO_2(w)_CNT and MnO_2(w)_CNT/Au are similar at 10 mV s^{-1}, 176 and 203 F g^{-1}, analogous to the values of 15 wt% MnO_2–CNT composite reported by Beguin and coworkers, 200–230 F g^{-1} measured at 2 mV s^{-1} [25], the capacitance value of 199 F g^{-1} reported for the MnO_2–CNT film on a Ta foil [26], less than 400 F g^{-1} of MnO_2–CNT film on a Ti/Si substrate [35].

We note the C_m value of MnO_2(w)_CNT decreases rapidly with increasing sweep rate, and that of MnO_2_MnO_2 decreases even faster. Evidently, the rapid decline results from the high resistance of MnO_2. Addition of the gold layer alleviates the negative influences of high resistance. Consequently, when the corresponding C_m values of two different stack layers are compared, the specific capacitance of Fe–Al/Au/Ti/SiO_2 is generally higher at high sweep rates, indicating a more conductive stack layer collects electrical charge more effectively.

The EIS results confirm the effects of MnO_2 and Fe–Al/SiO_2 on electrode resistance. Nyquist plots of bCNT and MnO_2–bCNT are compared in Fig. 4(a). Both curves are characterized with a depressed semicircle and a sloping line. As expected, the impedance of MnO_2–bCNT is higher than that of bCNT, owing to the presence of MnO_2. The electrode resistance may be symbolized by the magnitude of impedance at 1 kHz, equivalent series resistance (ESR). The ESR value of bCNT is 47.4 Ω cm^2, less than that of MnO_2–bCNT 102.1 Ω cm^2. Both ESR values are considered to be considerable. The relatively high resistances of bCNT and MnO_2–bCNT explain their rapidly decreasing C_m values with increasing sweep rate. In contrast, the ESR values of bCNT/Au and MnO_2–bCNT/Au are much less, 4.7 and 4.4 Ω cm^2, respectively. Fig. 4(b) shows the complex plane plots for bCNT/Au and MnO_2–bCNT/Au, featured with a dwindled semicircle and a steep line. Nonetheless, the electrode resistances of bCNT/Au and MnO_2–bCNT/Au are still higher than the ESR value of the asymmetric capacitor of MnO_2 and active carbon in the parallel plate configuration, <1.3 Ω cm^2 [36], and that of the composite of MnO_2 and CNT, 1.56 Ω cm^2 [37].

3.3. Power and energy output

Fig. 5(a) presents the discharge curves at 30 μA for CNT_CNT, MnO_2_MnO_2, and MnO_2(+)_CNT, recorded during the galvanostatic charge/discharge experiments. The discharge time is around 2.0 s for the cell voltage of CNT–CNT to drop from 1.0 to 0.0 V, since its capacitance is small. While the MnO_2(+)_CNT cell discharges its energy in 195.0 s, much longer than the other two cells. At the beginning of discharge, the IR drops of CNT_CNT and MnO_2_MnO_2 are substantial. In contrast, the IR drop of MnO_2(+)_CNT is quite

Table 1
Values of specific capacitance C_m of the comb-like working electrode. The voltammograms were recorded with one of the two comb-like electrodes designated as working electrode and the other as the counter electrode. The working electrode is marked with (w).

Sweep rate mV s^{-1}	CNT(w)_CNT (CNT(w)_CNT/Au) F g^{-1}	MnO_2(w)_CNT (MnO_2(w)_CNT/Au) F g^{-1}	MnO_2(w)_MnO_2 (MnO_2(w)_MnO_2/Au) F g^{-1}
10	36.5 (35.5)	176 (203)	61.1 (45.9)
50	19.8 (19.4)	55.5 (73.9)	8.2 (24.3)
200	10.0 (11.3)	8.5 (17.1)	7.2 (9.0)
500	3.3 (7.2)	2.0 (7.2)	1.9 (5.0)

On Fe–Al/SiO_2, the loading of CNT is 0.48 mg cm^{-2}, that of MnO_2–CNT 1.76 mg cm^{-2}; while on Fe–Al/Au/Ti/SiO_2, the loading of CNT is 0.23 mg cm^{-2}, and that of MnO_2–CNT 1.03 mg cm^{-2}. The capacitance values in parentheses are the results of Fe–Al/Au/Ti/SiO_2.

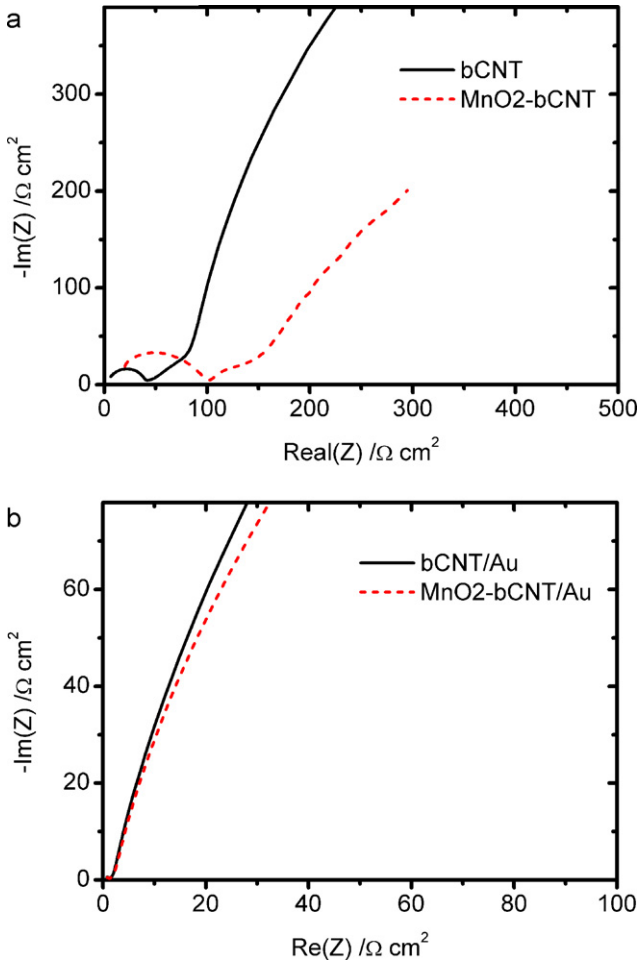

Fig. 4. Impedance results of (a) bCNT and MnO_2–bCNT; (b) bCNT/Au and MnO_2–bCNT/Au.

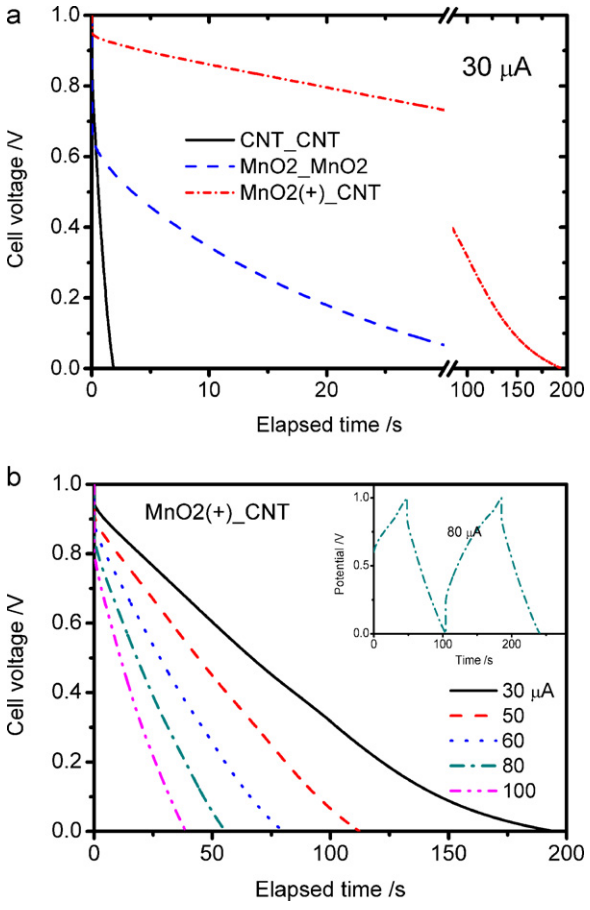

Fig. 5. Discharge curves of the three cells built on Fe–Al/SiO_2 in galvanostatic charge/discharge experiments. The cell voltage is plotted versus elapsed time for (a) CNT_CNT, MnO_2–MnO_2, MnO_2(+)_CNT at 30 μA, (b) the MnO_2(+)_CNT cell at 30–100 μA. The inset of (b) shows the typical charge and discharge curves of MnO_2(+)_CNT.

small. Fig. 5(b) shows the discharge curves of MnO_2(+)_CNT at higher currents. Its IR drop increases somewhat with increasing discharge current. The same trend of increasing IR drop is also observed in the other two cells, since a large initial voltage drop is required to drive a high discharge current. After the initial voltage drop, the cell voltage of MnO_2(+)_CNT decreases almost linearly with the elapsed time except the end of discharging.

The influences of a more conductive stack layer are shown in Fig. 6(a), which compares the discharge curves at 30 μA for the three cells built on Fe–Al/Au/Ti/SiO_2. The IR drop of MnO_2(+)_CNT/Au is similar to that of MnO_2(+)_CNT, while IR drops of the other two cells are less than those of their analogous cells in Fig. 5(a). The improvement on IR drop is most obvious on the MnO_2_MnO_2/Au cell because of the high resistance of MnO_2 phase. More discharge curves of the asymmetric cell MnO_2(+)_CNT/Au are plotted in Fig. 6(b). The discharge time of MnO_2(+)_CNT/Au is somewhat shorter than that of MnO_2(+)_CNT at the same discharge current.

Compared with the symmetric cells, the cell voltage of the two asymmetric cells with a positive MnO_2 electrode remains high during discharge. In this design, the CNT electrode acts as an auxiliary electrode, quick in response to balance the pseudocapacitive reaction on the MnO_2 surface. Hence the capacitance of MnO_2–CNT electrode is well exploited in the actions of charge/discharge. In

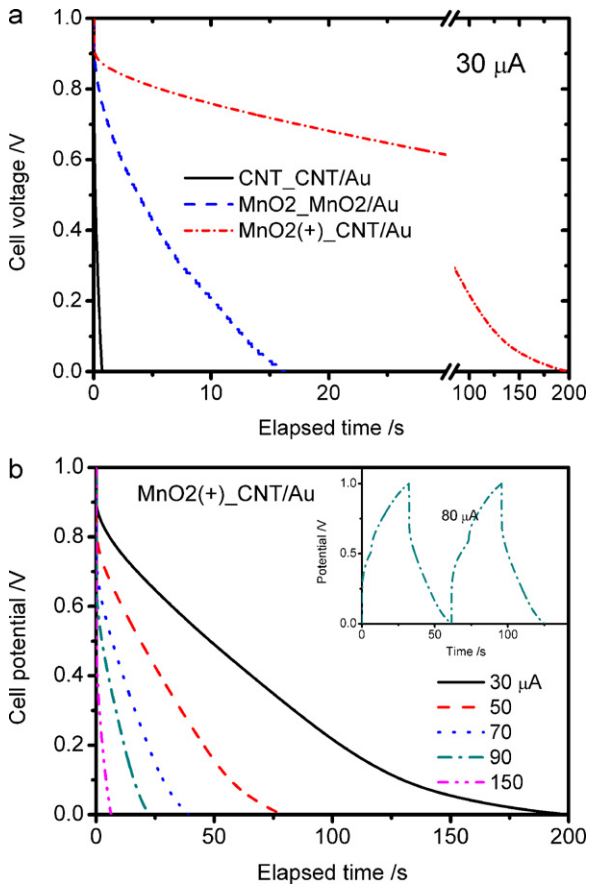

Fig. 6. Discharge curves of the three cells on Fe–Al/Au/Ti/SiO_2 in galvanostatic charge/discharge experiments. The cell voltage is plotted versus elapsed time for (a) CNT_CNT/Au, MnO_2–MnO_2/Au, MnO_2(+)_CNT/Au at 30 μA, (b) MnO_2(w)–CNT/Au at 30–150 μA. The inset of (b) shows the typical charge and discharge curves of MnO_2(w)–CNT/Au.

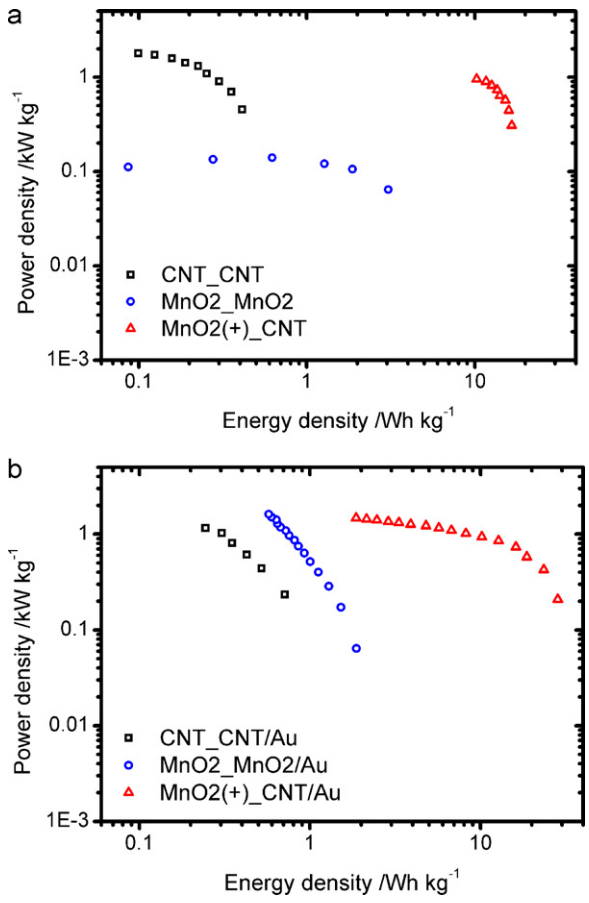

Fig. 7. Ragone plots for (a) the three cells built on Fe–Al/SiO_2, and (b) the three cells built on Fe–Al/Au/Ti/SiO_2.

contrast, the symmetric cell MnO_2_MnO_2 only utilizes a half capacitance of one MnO_2 electrode, since the two MnO_2 electrodes are in series. Likewise, CNT_CNT only utilizes a half capacitance of one CNT electrode, whose capacitance value is already less.

We calculate the energy output E_d of these single cells, based on their discharge curves of galvanostatic charge/discharge results.

$$E_d = I_d \int_0^{\Delta t_d} V_d(t)dt \quad (2)$$

in which I_d is the controlled discharge current, Δt_d is the discharge time for the cell voltage $V_d(t)$ to decrease from 1.0 to 0.0 V. We define the power output P_d as the energy output divided by the discharge time Δt_d,

$$P_d = \frac{E_d}{\Delta t_d} \quad (3)$$

Since the discharge power of a capacitor continuously decreases with its decreasing cell voltage, P_d is an average value of the discharge power. The energy and power densities are calculated by dividing the energy and power outputs by the total CNT and MnO_2 loadings of two comb-like electrodes.

Fig. 7(a) presents the log–log plots of specific power versus specific energy for CNT_CNT, MnO_2_MnO_2, and MnO_2(+)_CNT. Similar to other electrochemical capacitors, the energy density decreases with increasing power demand (or discharge current). Generally, the decrease in specific energy at low discharge current is less rapid than the decrease in specific energy at high current, resulting in the typical hook shape of Ragone plot. Since the CNT electrode is responsive but less capacitive, the CNT_CNT cell exhibits high power but low energy density. On the other hand, the MnO_2_MnO_2 cell displays low power and higher energy density because the MnO_2 electrode is pseudocapacitive but sluggish. Adopting one positive MnO_2 electrode, the MnO_2(+)_CNT cell acquires a significant gain in energy density at a trivial cost of power density.

Specific power and energy of CNT_CNT/Au, MnO_2_MnO_2/Au, and MnO_2(+)_CNT/Au are plotted in Fig. 7(b). These curves also display hook-shaped characteristics, and the asymmetric MnO_2(+)_CNT/Au cell exceeds the other two cells in energy performance. The specific values of power and energy in Fig. 7(b) are generally higher than those of their corresponding cells in Fig. 7(a), indicating a conductive stack layer accesses the stored charge more effectively.

Quantitatively, when MnO_2(+)_CNT discharges at the power level 0.96 kW kg^{-1}, its specific energy is 10.3 Wh kg^{-1}, equivalent to this single cell discharges at power output 34.6 μW and energy output 1340 μJ. For MnO_2(+)_CNT/Au, when it discharges at 1.16 kW kg^{-1}, its specific energy is 5.71 Wh kg^{-1}, equivalent to this single cell discharges at power output 23.6 μW with energy output 419 μJ. The performance of these two asymmetric cells is comparable to that of the miniature planar cell of conductive oxide RuO_2, prepared by direct write. The cell of two vertical RuO_2 plates, written on a quartz substrate, was reported to discharge at 1.10 W g^{-1} with a specific energy of 9.0 Wh kg^{-1} in aqueous 0.5 M H_2SO_4 [15]. In terms of power and energy per unit volume, MnO_2(+)_CNT discharges at energy density 3.38×10^{-3} Wh cm^{-3} and power density 0.314 W cm^{-3}; whereas MnO_2(+)_CNT/Au discharges at 2.57×10^{-2} Wh cm^{-3} and 5.20 W cm^{-3}. The energy and power densities of MnO_2(+)_CNT/Au are similar to those of the activated carbon micro-capacitor, but much lower than the 1 kW cm^{-3}

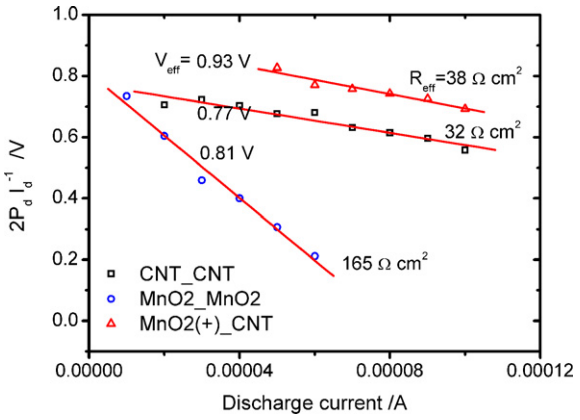

Fig. 8. Correlations of power output versus discharge current for the three cells on Fe–Al/SiO_2 with significant ohmic loss.

power of carbon-onion micro-capacitor, reported by Pech and coworkers. The working potential window of activated carbon and carbon-onion micro-capacitors was set at 3 V in the ionic liquid of Et_4NBF_4/propylene carbonate [38].

When the material costs of CNT and MnO_2 are not a primary concern, it could be more informative to report the performance based on the power and energy output data of single cell. Since all these cells are built on the same area, that comparison essentially assesses the performance on the basis of area, not mass. The discussion and detailed comparison are given in the supplementary data.

3.4. Electrode polarization loss

The power output of the above cells is generally less than that of an ideal capacitor. The non-ideal behavior is attributed to the electrode polarization loss, judging from the significant variation in CV capacitance with sweep rate. If the kinetic loss is negligible and the ohmic loss is predominant, according to Conway [39], the power output can be written as the product of a preset discharge current (I_d) and the current-driving voltage. The driving voltage is equal to an effective voltage (V_{eff}) diminished by the ohmic loss ($I_d R_{eff}$), in which R_{eff} is the effective resistance. Hence the variation of discharge power with respect to current is expressed as,

$$P_d = \frac{I_d(V_{eff} - I_d R_{eff})}{2} \quad (4)$$

If the power output obeys Eq. (4), a linear correlation of $2P_d\ I_d^{-1}$ versus I_d yields the effective cell resistance. Evidently R_{eff} is an oversimplified physical quantity that is distributive in nature, and varies with the time scale of discharge.

Fig. 8 shows that the $2P_d\ I_d^{-1}$ data of three cells built on Fe–Al/SiO_2 are well fitted in a linear correlation with respect to discharge current I_d. The correlated R_{eff} value is 32 Ω cm^2 for CNT_CNT, 165 Ω cm^2 for MnO_2_MnO_2, and 38 Ω cm^2 for MnO_2(+)_CNT. The high R_{eff} value of MnO_2_MnO_2 accounts for its low power density. The correlated R_{eff} values of MnO_2(+)_CNT and CNT_CNT also accurately reflects the fact that the power density of MnO_2(+)_CNT is slightly less than that of CNT_CNT.

4. Conclusions

We have prepared six electrochemical micro-capacitors of planar configuration using lithography and thin-film technologies. Among these capacitors, the asymmetric cells with a positive MnO_2–CNT electrode exhibit superior power and energy performance, indicating the importance of asymmetric configuration. The three cells on the Fe–Al/SiO_2 stack layer are featured with the well-defined but less conductive electrodes loaded with vertical CNT and MnO_2. In contrast, the cells on Fe–Al/Au/Ti/SiO_2 are built on the more conductive but less defined electrodes loaded with random CNT and less MnO_2. When the two asymmetric cells are compared, MnO_2(+)_CNT/Au is superior to MnO_2(+)_CNT in power density, but inferior in energy density.

Acknowledgements

The authors acknowledge the financial support of the National Science Council of Taiwan through the project NSC98-2221-E-011-028-MY2, and the assistance on equipment funding of National Taiwan University of Science and Technology on Nanotechnology Research.

Appendix A. Supplementary data

Supplementary data associated with this article can be found, in the online version, at doi:10.1016/j.jpowsour.2011.02.050.

References

[1] M. Inagaki, H. Konno, O. Tanaike, J. Power Sources 195 (2010) 7880–7903.
[2] Y. Zhang, H. Feng, X. Wu, L. Wang, A. Zhang, T. Xia, H. Dong, X. Li, L. Zhang, Int. J. Hydrogen Energy 34 (2009) 4889–4899.
[3] P.J. Hall, M. Mirzaeian, S.I. Fletcher, F.B. Sillars, A.J.R. Rennie, G.O. Shitta-Bey, G. Wilson, A. Cruden, R. Carter, Energy Environ. Sci. 3 (2010) 1238–1251.
[4] A.G. Pandolfo, A.F. Hollenkamp, J. Power Sources 157 (2006) 11–27.
[5] V.V.N. Obreja, Phys. E 40 (2008) 2596–2605.
[6] M. Kaempgen, C.K. Chan, J. Ma, Y. Cui, G. Gruner, Nano Lett. 9 (2009) 1872–1876.
[7] J.H. Sung, S.J. Kim, S.H. Jeong, E.H. Kim, K.H. Lee, J. Power Sources 162 (2006) 1467–1470.
[8] P.C. Chen, G. Shen, S. Sukcharoenchoke, C. Zhou, Appl. Phys. Lett. 94 (2009) 043113.
[9] A.L.M. Reddy, F.E. Amitha, I. Jafri, S. Ramaprabhu, Nano Res. Lett. 3 (2008) 145–151.
[10] P.C. Chen, G. Shen, Y. Shi, H. Chen, C. Zhou, ACS Nano 4 (2010) 4403–4411.
[11] D. Pech, M. Brunet, P.L. Taberna, P. Simon, N. Fabre, F. Mesnilgrente, V. Conedera, H. Durou, J. Power Sources 195 (2010) 1266–1269.
[12] C.C. Liu, D.S. Tsai, D. Susanti, W.C. Yeh, Y.S. Huang, F.J. Liu, Electrochim. Acta 55 (2010) 5768–5774.
[13] M. Beidaghi, W. Chen, C. Wang, J. Power Sources 196 (2011) 2403–2409.
[14] J. Chmiola, C. Largeot, P.-L. Taberna, P. Simon, Y. Gogotsi, Science 23 (2010) 480–483.
[15] C.B. Arnold, R.C. Wartena, K.E. Swider-Lyons, A. Pique, J. Electrochem. Soc. 150 (2003) A571–A575.
[16] C.B. Arnold, T.E. Sutto, H. Kim, A. Pique, Laser Focus World 40 (2004) S9–S13.
[17] S.C. Pang, M.A. Anderson, T.W. Chapman, J. Electrochem. Soc. 147 (2000) 444–450.
[18] L. Athouel, F. Moser, R. Dugas, O. Crosnier, D. Belanger, T. Brousse, J. Phys. Chem. C 112 (2008) 7270–7277.
[19] Y. Wang, A. Yuan, X. Wang, J. Solid State Electrochem. 12 (2008) 1101–1107.
[20] V. Khomenko, E. Raymundo-Pinero, F. Beguin, J. Power Sources 153 (2006) 183–190.
[21] X.H. Yang, Y.G. Wang, H.M. Xiong, Y.Y. Xia, Electrochim. Acta 53 (2007) 752–757.
[22] C. Ye, Z.M. Lin, S.Z. Hui, J. Electrochem. Soc. 152 (2005) A1272–A1278.
[23] M. Toupin, T. Brousse, D. Belanger, Chem. Mater. 14 (2002) 3946–3952.
[24] M. Toupin, T. Brousse, D. Belanger, Chem. Mater. 16 (2004) 3184–3190.
[25] E. Raymundo-Pinero, V. Khomenko, E. Frackowiak, F. Beguin, J. Electrochem. Soc. 152 (2005) A229–A235.
[26] H. Zhang, G. Cao, Z. Wang, Y. Yang, Z. Shi, Z. Gu, Nano Lett. 8 (2008) 2664–2668.
[27] G.M. Jacob, Q.M. Yang, I. Zhitomirsky, J. Appl. Electrochem. 39 (2009) 2579–2585.
[28] G.R. Li, Z.P. Feng, Y.N. Ou, D. Wu, R. Fu, Y.X. Tong, Langmuir 26 (2010) 2209–2213.
[29] A.L.M. Reddy, M.M. Shaijumon, S.R. Gowda, P.M. Ajayan, J. Phys. Chem. C 114 (2010) 658–663.
[30] T. Komukai, K. Aoki, H. Furuta, M. Furuta, K. Oura, T. Hirao, Jpn. J. Appl. Phys. 45 (2006) 6043–6045.
[31] T. Komukai, K. Aoki, H. Furuta, M. Furuta, K. Oura, T. Hirao, Jpn. J. Appl. Phys. 45 (2006) 8988–8990.
[32] JCPDS card no. 81-2261. International Center for Diffraction Data: Newtown Square, PA.
[33] JCPDS card no. 04-0784. International Center for Diffraction Data: Newtown Square, PA.
[34] S. Devaraj, N. Munichandraiah, J. Phys. Chem. C 112 (2008) 4406–4417.
[35] D.D. Zhao, Z. Yang, E.S.W. Kong, C.L. Xu, Y.F. Zhang, J. Solid State Electrochem., in press, doi:10.1007/s10008-010-1182-x.

[36] T. Brousse, P.L. Taberna, O. Crosnier, R. Dugas, P. Guillemet, Y. Scudeller, Y. Zhou, F. Favier, D. Belanger, P. Simon, J. Power Source 173 (2007) 633–641.
[37] V. Khomenko, E. Raymundo-Pinero, E. Frackowiak, F. Beguin, Appl. Phys. A 82 (2006) 567–573.
[38] D. Pech, M. Brune, H. Durou, P. Huang, V. Mochalin, Y. Gogotsi, P.-L. Taberna, P. Simon, Nat. Nanotechnol. 5 (2010) 651–654.
[39] B.E. Conway, Electrochemical Supercapacitors: Scientific Fundamentals and Technological Applications, Kluwer Academic Publishers/Plenum, New York, 1999, ch. 15, pp. 417–477.